# A Reaction-Diffusion Model of Cancer Invasion

## Robert A. Gatenby[1] and Edward T. Gawlinski

*Department of Diagnostic Imaging, College of Medicine [R. A. G.] and Department of Physics [E. T. G.], Temple University, Philadelphia, Pennsylvania 19122*

## Abstract

We present mathematical analyses, experimental data, and clinical observations which support our novel hypothesis that tumor-induced alteration of microenvironmental pH may provide a simple but complete mechanism for cancer invasion. A reaction-diffusion model describing the spatial distribution and temporal development of tumor tissue, normal tissue, and excess $H^+$ ion concentration is presented. The model predicts a pH gradient extending from the tumor-host interface, which is confirmed by reanalysis of existing experimental data. Investigation of the structure and dynamics of the tumor-host interaction within the context of the model demonstrates a transition from benign to malignant growth analogous to the adenoma-carcinoma sequence. The effect of biological parameters critical to controlling this transition are supported by experimental and clinical observations. Tumor wave front velocities determined via a marginal stability analysis of the model equations are consistent with in vivo tumor growth rates. The model predicts a previously unrecognized hypocellular interstitial gap at the tumor-host interface which we demonstrate both *in vivo* and *in vitro*. A direct correlation between the interfacial morphology and tumor wave front velocity provides an explicit, testable, clinically important prediction.

## I. Introduction

We mathematically model tumor invasion in an attempt to find a common, underlying mechanism by which primary and metastatic cancers invade and destroy normal tissues. In this approach we make no assumptions about the process of carcinogenesis. That is, we are not modeling the genetic changes which result in transformation nor do we seek to understand the causes of these changes. Similarly, we do not attempt to model the large-scale morphological features of tumors such as central necrosis. Rather, we concentrate on the microscopic scale population interactions occurring at the tumor-host interface, reasoning that these processes strongly influence the clinically significant manifestations of invasive cancer.

Any broadly applicable model must incorporate as key parameters properties common to all or nearly all tumors despite their underlying genetic instability and heterogeneity (1–5). We note that one consistent cellular dynamic is evolution of tumor populations away from the differentiated state of the tissue of origin toward one that is more primitive and less ordered (6–10). Metabolic changes parallel this evolution with increasing use of glycolytic metabolism (even in the presence of oxygen) despite the 19-fold decrease in energy production that results (10).

We propose the simple hypothesis (11–13) that it is precisely this inefficiency which may facilitate successful tumor invasion. Specifically, we hypothesize that transformation-induced reversion of neoplastic tissue to primitive glycolytic metabolic pathways, with resultant increased acid production and the diffusion of that acid into surrounding healthy tissue, creates a peritumoral microenvironment in which tumor cells survive and proliferate, whereas normal cells are unable to remain viable. The following temporal sequence would ensue: (a) high $H^+$ ion concentrations in tumors will extend, by

chemical diffusion, as a gradient into adjacent normal tissue, exposing these normal cells to tumor-like interstitial pH; (b) normal cells immediately adjacent to the tumor edge are unable to survive in this chronically acidic environment; and (c) the progressive loss of layers of normal cells at the tumor-host interface facilitates tumor invasion.

Key elements of this tumor invasion mechanism are low interstitial pH of tumors due to primitive metabolism and reduced viability of normal tissue in a pH environment favorable to tumor tissue. The first element is supported by clinical data showing that tumors in situ use approximately one order of magnitude more glucose than normal tissue (14–16) and that tumor interstitial pH is typically 0.5 units lower than normal tissue (17–21). The second element is supported by studies (22–27) showing that normal cells have an optimal $pH_e$ of 7.4 with a sharp decline in viability below $pH_e$ of 7.1, whereas tumor cells typically proliferate optimally at a pH of 6.8.[2] Indeed, Dairkee et al. (28) have recently used this differential sensitivity to suppress the growth of normal cells in human breast biopsies, allowing selective isolation of tumor populations. Finally, data reported by Martin and Jain (29) and Martin (Ref. 30; personal communication) demonstrate a pH gradient extending from a tumor edge into surrounding normal tissue with the pH in peritumoral normal tissue significantly lower than 7.1.

In this article, we mathematically frame our acid mediation hypothesis as a system of reaction-diffusion equations which, when solved, make detailed predictions of the structure and dynamics of the tumor-host interface. These model equations depend only on a small number of cellular and subcellular parameters. Analysis of the equations shows that the model predicts a crossover from a benign tumor to one that is aggressively invasive as a dimensionless combination of the parameters increases through a critical value. We show that changes to these basic biological parameters resulting in such a transition are consistent with those observed experimentally and clinically in transformation from adenoma or carcinoma in situ to invasive cancer.

We quantify the size of the $H^+$ ion gradient extending into the normal tissue and find it is consistent with published data. The dynamics and structure of the tumor-host interface in invasive cancers are shown to be controlled by the same biological parameters which generate the transformation from benign to malignant growth. A hypocellular interstitial gap at the interface is predicted to occur in some cancers. We present evidence of this heretofore unrecognized phenomenon in human tumors and in *in vitro* coculture experiments. Finally, our mathematical model demonstrates a strong correlation between the interfacial morphology and the rate of tumor growth, providing an explicit, testable clinical prediction.

## II. Description of the Model

We present a mathematical model of the tumor-host interface based on our acid mediation hypothesis of tumor invasion. It is important to

---

[2] At least three mechanisms act to reduce normal cell viability *in vivo* at low pH: (a) Nonmalignant cells are unable to maintain intracellular pH when the extracellular pH drops below 7.1, having multiple consequences including precipitous reduction in the activity of phosphofructokinase—the rate-limiting enzyme in glucose metabolism (23, 25, 26). (b) Acidic pH causes fibroblasts and macrophages to release lysosomal enzymes, leading to a breakdown of extracellular matrix in peritumoral normal tissue (31). (c) Acidic pH markedly reduces the number and patency of gap junctions, thus limiting the ability of normal tissue to cooperatively maintain the viability of normal cells at the tumor-host interface (32, 33).

point out that we are neither modeling early tumor formation (oncogenesis) nor large-scale tumor morphological structures such as central necrosis. Our model describes the interaction between a growing tumor and surrounding normal tissue only in the immediate vicinity of the tumor-host interface.

The model is a system of three coupled reaction-diffusion equations which determine the spatial distribution and temporal evolution of three fields: $N_1$ $(x, t)$, the density of normal tissue; $N_2$ $(x, t)$, the density of neoplastic tissue; and $L$ $(x, t)$, the excess concentration of $H^+$ ions. The units of $N_1$ and $N_2$ are cells/cm$^3$ and excess $H^+$ ion concentration is expressed as a molarity (M). $x$ and $t$ are the position (in cm) and time (in s), respectively.

The behavior of the normal tissue is determined by (a) the logistic growth of $N_1$ with growth rate $r_1$ and carrying capacity $K_1$; (b) a population competition with the tumor tissue characterized by a Lotka-Volterra competition strength parameter $\alpha_{12}$; (c) the interaction of $N_1$ with excess $H^+$ ions leading to a death rate proportional to $L$; and (d) cellular diffusion with an $N_2$-dependent diffusion coefficient, $D_{N_1}[N_2]$. These effects can be written as the following reaction-diffusion equation:

$$\frac{\partial N_1}{\partial t} = r_1 N_1 \left(1 - \frac{N_1}{K_1} - \alpha_{12} \frac{N_2}{K_2}\right) - d_1 L N_1 + \nabla \cdot (D_{N_1}[N_2]\nabla N_1)$$

(A)

$d_1 L$ is the excess acid concentration dependent death rate in accord with the well-described decline in the growth rate of normal cells due to the reduction of pH from its optimal value of 7.4.[3] $r_1$ has units of 1/s, $K_1$ and $K_2$ have units of cells/cm$^3$, $d_1$ has units of 1/(M · s), and $\alpha_{12}$ is dimensionless. Normal tissue is only able to diffuse into regions where $N_2$ is small due to a volume exclusion effect; thus, the $N_2$ dependence of the normal tissue diffusion coefficient, $D_{N_1}$.

The neoplastic tissue growth is described by a similar reaction-diffusion equation with one important difference, the lack of a death term due to the excess acid. Thus,

$$\frac{\partial N_2}{\partial t} = r_2 N_2 \left(1 - \frac{N_2}{K_2} - \alpha_{21} \frac{N_1}{K_1}\right) + \nabla \cdot (D_{N_2}[N_1]\nabla N_2)$$

(B)

where $r_2$ and $K_2$ are the growth rate and carrying capacity of the neoplastic tissue and $\alpha_{21}$ is the competition parameter characterizing the tumor tissue growth reduction due to competition with the normal tissue for space and other resources. No acid concentration-dependent death rate is included in Eq. B because no decline in the growth rate of tumor cells has been observed at the pH levels to be examined.[3]

We now make the following simplifying assumptions:

$$D_{N_1}[N_2] = 0 \quad \text{and} \quad D_{N_2}[N_1] = D_2(1 - N_1/K_1)$$

(C)

The first equation in Eq. C is a recognition that the healthy tissue is well regulated and participating normally in an organ and will, therefore, not be diffusing in space. In the second equation in Eq. C, $D_2$ is the diffusion constant (cm$^2$/s) for neoplastic tissue in the absence of healthy tissue. Therefore, when the local healthy tissue concentration is at its carrying capacity, the diffusion coefficient for neoplastic tissue is zero and the tumor is confined. The latter mechanism is at the heart of the model; the neoplastic tissue is unable to spread without

the surrounding healthy tissue being first diminished from its carrying capacity, i.e., it is assumed that fully healthy tissue ($N_1 = K_1$) is able to marshal multiple defense mechanisms (immunological and nonimmunological) to keep the tumor confined. Since healthy tissue is by definition at its carrying capacity and thus occupies all available space within the volume of tissue adjacent to the tumor, it is only into regions where healthy tissue number density has been significantly reduced that tumor tissue can effectively spread. Eq. C is the simplest possible assumption which phenomenologically model these aspects of the tumor-host interaction.

It is assumed that excess $H^+$ ions are produced at a rate proportional to the neoplastic cell density and diffuse chemically. An uptake term is included to take account of the mechanisms for increasing local pH (e.g., buffering and large-scale vascular evacuation). Therefore, we have the following equation governing the excess $H^+$ ion concentration:

$$\frac{\partial L}{\partial t} = r_3 N_2 - d_3 L + D_3 \nabla^2 L$$

(D)

where $r_3$ is the production rate (M · cm$^3$/(cell · s)), $d_3$ is the reabsorption rate (1/s), and $D_3$ is the $H^+$ ion diffusion constant (cm$^2$/s).

In the analysis presented below, it will be shown that, for a certain range of parameters, there are spatial regions where $N_1$ and $N_2$ can stably coexist; therefore, there is the potential for competition for space and resources between these two populations. In such a situation, the Lotka-Volterra parameters $\alpha_{12}$ and $\alpha_{21}$ will be important for a quantitative description of the tumor-host interface. Nevertheless, in the remainder of this article we restrict ourselves to the case where $\alpha_{12} = \alpha_{21} = 0$. As will be shown below, for aggressively invasive cancers there is no region of coexistence between tumor and normal tissues and therefore the Lotka-Volterra competition has no effect on the structure and dynamics of the tumor-host interface. The restriction that $\alpha_{12} = 0$ and $\alpha_{21} = 0$ in no way changes the qualitative behavior of the model but it does facilitate the derivation of analytical results useful for understanding frankly invasive tumors.

The following transformation of variables renders Eqs. A–D dimensionless:

$$\eta_1 = \frac{N_1}{K_1} \qquad \eta_2 = \frac{N_2}{K_2} \qquad \Lambda = \frac{L}{L_0}$$

$$\tau = r_1 t \qquad \xi = \sqrt{\frac{r_1}{D_3}} x$$

(E)

where $L_0 = r_3 K_2/d_3$. Using the transformations in Eq. E, the dimensionless form of the equations become:

$$\frac{\partial \eta_1}{\partial \tau} = \eta_1(1 - \eta_1) - \delta_1 \Lambda \eta_1$$

(F)

$$\frac{\partial \eta_2}{\partial \tau} = \rho_2 \eta_2(1 - \eta_2) + \nabla_\xi \cdot [\Delta_2(1 - \eta_1)\nabla_\xi \eta_2]$$

(G)

and

$$\frac{\partial \Lambda}{\partial \tau} = \delta_3(\eta_2 - \Lambda) + \nabla_\xi^2 \Lambda$$

(H)

where

$$\delta_1 = (d_1/d_3) \times (r_3/r_1) \times K_2$$

$$\rho_2 = r_2/r_1$$

$$\Delta_2 = D_2/D_3$$

$$\delta_3 = d_3/r_1 \qquad \text{(I)}$$

are the four dimensionless quantities which parameterize the model. Eqs. F and G now explicitly include the simplifying assumptions given in Eq. C and $\alpha_{12} = \alpha_{21} = 0$ as well.

## III. Prediction of Benign to Malignant Crossover with Clinical Correlations

The fixed points (spatial homogeneity and temporal invariance) of the model are found by setting the spatial and temporal derivatives in Eqs. F–H to zero and solving for the fields. The following four fixed points are thus obtained:

$$\begin{array}{llll}
\text{FP 1:} & \eta_1^* = 0 & \eta_2^* = 0 & \Lambda^* = 0 \\[4pt]
\text{FP 2:} & \eta_1^* = 1 & \eta_2^* = 0 & \Lambda^* = 0 \\[4pt]
\text{FP 3:} & \eta_1^* = 1 - \delta_1 & \eta_2^* = 1 & \Lambda^* = 1 \\[4pt]
\text{FP 4:} & \eta_1^* = 0 & \eta_2^* = 1 & \Lambda^* = 1 \quad \text{(J)}
\end{array}$$

These correspond to four physical states: FP 1, the trivial absence of all tissues and acid; FP 2, the healthy tissue existing at its carrying capacity in the absence of tumor tissue and acid; FP 3, the coexistence of tumor tissue at its carrying capacity and healthy tissue at a diminished level; and FP 4, the tumor tissue existing at its carrying capacity having killed off all healthy tissue.

A linear stability analysis (34) shows that FP 1 and FP 2 are unconditionally unstable, i.e., small perturbations in $\eta_1$ and $\eta_2$ in the case of FP 1 or small perturbations in $\eta_2$ alone in the case of FP 2 will continue to grow until the system evolves toward one of the other two stable fixed points (either FP 3 or FP 4). The linear stability analysis also shows that FP 4 is stable and FP 3 is unstable when $\delta_1 > 1$ and vice versa when $\delta_1 < 1$. Two important consequences follow from this analysis: (a) If a spatial region occupied by the system in one of the stable fixed points is adjacent to one at an unstable fixed point, the stable region will grow into the unstable region in the form of a traveling wave front. (b) If a tumor evolves such that $\delta_1$ increases through unity, the dynamics and structure of that tumor will crossover from FP 3 to FP 4.[4]

This analysis results in several biologically significant predictions. First, we find that some tumors should be populated by a variable, but nonzero, fraction of genotypically normal cells. Although a novel concept, there are some supporting data showing that benign tumors are polyclonal and contain sections of histologically benign tissue (35–37).

Second, the prediction of a crossover from FP 3 to FP 4 as $\delta_1$ increases through unity is also biologically significant. In terms of the basic system parameters, the dimensionless $\delta_1$ is given by $\delta_1 = (d_1/d_3) \times (r_3/r_1) \times K_2$. The tumorigenic transformations that a cell undergoes will not affect either $r_1$ or $d_1$ (these characterize the healthy tissue only). Changes to the other three parameters causing $\delta_1$ to increase through unity are consistent with the following three clinical observations:

1. $\delta_1$ will increase linearly with the value of $K_2$, the carrying capacity of the tumor population. Studies by Folkman and colleagues

(38, 39) show that initial tumor growth is avascular. The resulting limited nutrient supply reduces $K_2$ and, as predicted by the model, tumor growth is limited. However, acquisition of angiogenesis (increasing $K_2$ because of greater substrate availability) results in invasive tumor growth.

2. $\delta_1$ will increase with increasing $r_3$, the production rate of acid by the tumor. Thus, tumor growth is predicted to be more aggressive as the tumor becomes more glycolytic, consistent with studies (14–16) that show malignant tumors take up more glucose than benign tumors and that among malignant tumors increased uptake of glucose strongly correlates with poorer patient prognosis.

3. $\delta_1$ will increase as $d_3$, the reabsorption rate of acid, decreases, predicting that tissue environments in which acid washout is diminished are permissive for malignant growth. Although this prediction has not been explicitly tested, states of vascular disruption such as chronic scarring and inflammation (e.g., cirrhosis and ulcerative colitis) tend to be sites predisposed to cancers (37).

On the basis of the above clinical correlations, we are naturally led to identify the crossover at $\delta_1 = 1$ with the transformation of noninvasive tumors, such as adenoma and carcinoma in situ ($\delta_1 < 1$), into frankly invasive malignant tumors ($\delta_1 > 1$).

## IV. Experimental Evidence Consistent with the Acid Mediation Model

In recent articles, Martin and Jain (29) and Martin (Ref. 30; personal communication) reported in vivo interstitial pH profiles for both neoplastic (VX2 rabbit carcinoma) and peritumoral normal tissue. Using the model presented in the preceding section, we reanalyzed their raw data (29, 30) to extract estimates of the parameters $r_3$ and $d_3$ in Eq. D. Our reanalysis shows their data to be consistent with the acid mediation model by both confirming the existence of a pH gradient extending into peritumoral normal tissue and deriving independent yet equivalent acid production rates.

The Martin-Jain (29) data consist of pH measurements taken at a variety of points within both the tumor and surrounding healthy tissue for four composite cases. In the data sets, the tumor sites are at a lower pH than the normal tissue sites and there appears to be a relatively smooth pH gradient extending from the tumor edge into the surrounding normal tissue. To quantify this gradient, we calculated the distance, $r$, between the tumor centroid and each normal site. In Fig. 1 we plot the excess $H^+$ ion concentration, $L$, for these sites versus $r$,
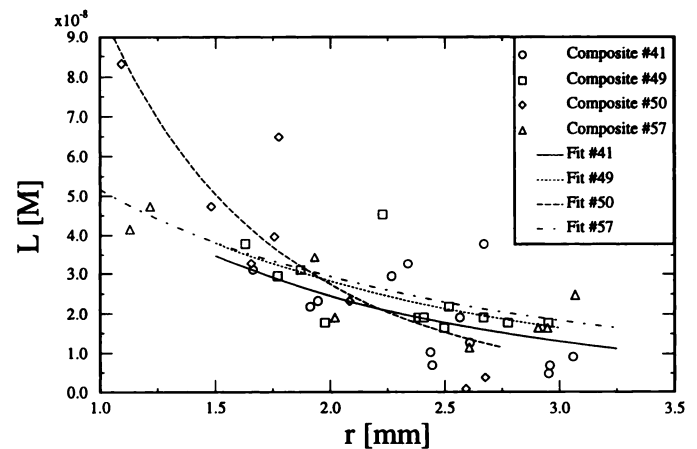


Fig. 1. Excess $H^+$ ion concentration, $L$, plotted as a distance, $r$, from tumor centroid. The plotting symbols are the data of Martin (30) converted from absolute pH to excess $H^+$ ion concentration and x-y coordinates to distance from tumor centroid. Note the pronounced spatial gradient in the $H^+$ ion concentration at increased distance from the tumor. The lines are the curve fits of the data points to Eq. L. See Table 1 for the values of the fitting coefficients.

---

[4] With the inclusion of the Lotka-Volterra terms discussed above, this crossover point shifts from $\delta_1 = 1$ to $\delta_1 = 1 - \alpha_{12}$, and the values of FP 3 change to reflect their dependence on $\alpha_{12}$ and $\alpha_{21}$. However, all qualitative features of the model are unchanged.

Table 1 *Determinations of $d_3$, $r_3$, and $r_0$ for the four Martin (30) data sets*

Estimates of parameters $r_3$ and $d_3$ determined by fitting Eq. L to a converted form of the data of Martin and Jain (29). Tumor radius $r_0$ is reported incidentally as well. See Fig. 1 for curve fits.

| Composite | $d_3$ | $r_3$ | $r_0$ (mm) |
|---|---|---|---|
| 41 | $1.03 \times 10^{-4}$/s | $1.83 \times 10^{-17}$ M · cm$^3$/(s · cell) | 1.23 |
| 49 | $6.66 \times 10^{-5}$/s | $1.17 \times 10^{-17}$ M · cm$^3$/(s · cell) | 1.28 |
| 50 | $4.60 \times 10^{-4}$/s | $1.78 \times 10^{-16}$ M · cm$^3$/(s · cell) | 1.07 |
| 57 | $4.47 \times 10^{-5}$/s | $6.17 \times 10^{-18}$ M · cm$^3$/(s · cell) | 1.52 |
| Geometric mean | $1.09 \times 10^{-4}$/s | $2.20 \times 10^{-17}$ M · cm$^3$/(s · cell) | |

assuming a baseline of pH = 7.4 for healthy tissue. It is apparent from this figure that excess H$^+$ ion concentration diminishes markedly from $L \approx 8 \times 10^{-8}$ M (pH = 6.9) to $L \approx 0.5 \times 10^{-8}$ M (pH = 7.3), with increasing distance from the tumor. This observation is fully consistent with our hypothesis, and, in what follows, we will use it to obtain estimates for the acid production and washout rates.

The data depicted in Fig. 1 are analyzed within the context of our model by using Eq. D and making the following assumptions: (a) the left-hand side of Eq. D is set to zero because the pH profile evolves very slowly on the time scale of the pH measurements; (b) the Laplacian in Eq. D is two-dimensional because the rabbit ear chamber used (29) was extremely thin, effectively confining the tissues to a plane; (c) the tumor exists at its carrying capacity $K_2$; and (d) the tumor-host interface is smooth and sharp (on the length scale of the entire tumor). With these assumptions we rewrite Eq. D as:

$$r_3 K_2 - d_3 L + \frac{D_3}{r} \frac{\partial}{\partial r}\left( r \frac{\partial L}{\partial r} \right) = 0 \quad r < r_0$$

$$- d_3 L + \frac{D_3}{r} \frac{\partial}{\partial r}\left( r \frac{\partial L}{\partial r} \right) = 0 \quad r \geq r_0 \qquad \text{(K)}$$

where $r_0$ is the tumor radius. Eq. K is subject to the boundary conditions that $\lim_{r \to \infty} L(r) = 0$ and that $L(r)$ and its derivative are continuous at $r_0$. Subject to these conditions, Eq. K has the following solution:

$$L(r) = L_0[1 - qr_0 K_1(qr_0) I_0(qr)] \quad r < r_0$$

$$L(r) = qr_0 L_0 I_1(qr_0) K_0(qr) \quad r \geq r_0 \qquad \text{(L)}$$

where $q = \sqrt{d_3/D_3}$, $L_0 = r_3 K_2/d_3$, and $I_{0,1}$ and $K_{0,1}$ are modified Bessel functions. The biological significance of $q$ and $L_0$ is as follows: $q$ is the reciprocal of the length scale characterizing the H$^+$ ion gradient across the tumor-host interface, and $L_0$ is the excess H$^+$ ion concentration asymptotically deep within a large tumor.

Eq. L can be curve fitted to the converted data shown in Fig. 1 for estimates of $q$, $r_0$, and $L_0$. In turn, estimates of $r_3$ and $d_3$ can be found using $r_3 = L_0 q^2 D_3/K_2$ and $d_3 = q^2 D_3$. In Table 1 we show the results for such a determination of $r_0$, $r_3$, and $d_3$ for the four Martin-Jain (29) data sets. Martin and Jain (29) estimated acid production by tumor tissue in a quite different fashion, i.e., by fitting their data to a one-dimensional diffusion model along a line joining two adjacent blood vessels. They find an acid production rate of $Q = 3.29 \times 10^{-7}$ M/s which compares reasonably well with our value of $Q = r_3 K_2 = 2.2 \times 10^{-8}$ M/s[5] considering that (a) we analyze the acid gradient outside the tumor whereas they analyze it between adjacent blood vessels entirely within the tumor, and (b) acid removal in our model is accomplished with an explicit acid washout term ($d_3$),

whereas they impose constant H$^+$ ion concentration boundary conditions at the vessel walls.

## V. Solutions of the Model and the Resultant Biological Predictions

We have performed computer simulations of our model by numerically solving Eqs. F–H using suitable boundary and initial conditions.[6] Biological parameter values are shown in Table 2. We present two such simulations: the first with $\delta_1 = 12.5 > 1$ (FP 4 dynamics, i.e., malignant) and the second with $\delta_1 = 0.5 < 1$ (FP 3 dynamics, i.e., benign). In both cases the remaining parameters are as follows: $\rho_2 = 1.0$, $\Delta_2 = 4.0 \times 10^{-5}$, and $\delta_3 = 70.0$. The dimensionless system size was taken to be $2\Xi = 2.5$, where $-\Xi \leq \xi \leq \Xi$ and the spatial and temporal discretizations used were $\Delta\xi = 0.01$ and $\Delta\tau = 0.01$.

In Fig. 2 we plot the numerical solutions (——, - - - - -, - - -) for the late-time wave front profiles for both cases. In Fig. 2 the wave fronts are propagating from *left to right*. When $\delta_1 > 1$, the normal tissue is completely destroyed behind the advancing wave front (Fig. 2a). When $\delta_1 < 1$, however, the tumor and healthy tissue coexist behind the wave front (Fig. 2b) but with the latter at a diminished concentration $\eta_1 = 1 - \delta_1$. Notice that for the case where $\delta_1 > 1$, the healthy tissue profile leads the tumor edge, resulting in a hypocellular interstitial gap, whereas for $\delta_1 < 1$ it is coincident with the tumor edge. In the former case, this offset is approximately given by Eq. O and is consistent with clinical pathology findings (see Figs. 4 and 5). Finally, note that the H$^+$ ion profile is centered, as expected, on the very sharp tumor edge.

Although we are able to numerically solve our model equations, it is highly desirable to obtain a general understanding of the sensitivity of relevant biological quantities to changes in the basic system parameters. To gain insight into such sensitivities, we have constructed approximate mathematical solutions to the model equations. Once obtained, these analytical results are used to make specific biological predictions concerning the dependence of the structure and dynamics of the tumor-host interface on the basic system parameters. The accuracy of these solutions is apparent by comparing them with the numerical solutions (see Fig. 2 and Table 3). The mathematically inclined reader may wish to consult the "Appendix" for the details of these solutions; however, in what follows we simply present a summary of the resultant predictions.

The interfacial widths of acid and tumor tissue profiles can be determined by performing the integrals in Eqs. A5 and A6 using Eqs. A2 and A3. Doing so, we find the following interfacial widths:

$$W_\Lambda = \sqrt{\frac{2}{\delta_3}} \qquad \text{(M)}$$

and

$$W_{\eta_2} = \frac{\pi c}{\sqrt{3}\rho_2} \qquad \text{(N)}$$

where $c$ is the speed of the propagating wave front. Because of the complexity of the analytical solution in Eq. A4, no such simple result is derivable for the width of the normal tissue profile, $W_{\eta_1}$. Instead, we numerically performed the integrals in Eqs. A5 and A6 for the two values of $\delta_1$ and present the results in Table 3.

As is apparent in Fig. 2a, when $\delta_1$ increases beyond unity, an appreciable hypocellular interstitial gap develops between the advancing tumor edge and the retreating healthy tissue. In general, no simple

---

[5] In obtaining this value, we have used the same acid diffusion constant as Martin and Jain (29) rather than the value appearing in Table 2.

[6] E. T. Gawlinski, R. A. Gatenby, and Y. Guan. Marginal stability velocity in model of cancer invasion, manuscript in preparation.

Table 2 *Parameter values used in model Eqs. A–D and references used in determining their values*

| Parameter | Estimate | Reference |
|---|---|---|
| $K_1$ | $5 \times 10^7/cm^3$ | 46 |
| $K_2$ | $5 \times 10^7/cm^3$ | 46 |
| $r_1$ | $1 \times 10^{-6}/s$ | 46 |
| $r_2$ | $1 \times 10^{-6}/s$ | 46 |
| $D_2$ | $2 \times 10^{-10} cm^2/s$ | 47 |
| $D_3$ | $5 \times 10^{-6} cm^2/s$ | 48 |
| $r_3$ | $2.2 \times 10^{-17} M \cdot cm^3/s$ | From Table 1 |
| $d_3$ | $1.1 \times 10^{-4}/s$ | From Table 1 |
| $d_1$ | $0 \Rightarrow 10/M \cdot s$ | |

analytical result is obtainable for the dependence of this gap, $\xi_0$, on the system parameters except for when $\delta_1 \gg 1$, in which case:

$$\xi_0 \approx \frac{Log\left[\dfrac{\delta_1}{2}\right]}{\sqrt{\delta_3}} + \sqrt{\frac{c}{\sqrt{\delta_3}}} \qquad \delta_1 \gg 1 \qquad (O)$$

In Fig. 3 we show exact values of $\xi_0$ for the full range of $\delta_1$ determined by numerically integrating Eq. A5 with $f(\zeta)$ given by Eq. A4.

To compute the positions of the plotting symbols in Fig. 2, we used Eqs. A2–A4, with a value of $c$ determined from the numerical solutions themselves. If we compute an analytical expression for $c$ in terms of the basic system parameters, our model equations would be completely solved. Such an analytical result for $c$ can be obtained by performing a "marginal stability analysis" (40–43). For our model, this is a rather technical calculation, the details of which will be published elsewhere.[6] The result of this analysis is a transcendental equation for $c$, namely,

$$c = \Delta_2 \eta_1'(\zeta = 0; c) + 2\sqrt{\{1 - \eta_1(\zeta = 0; c)\}\rho_2\Delta_2} \qquad (P)$$

where $\eta 1$ and its derivative are evaluated at $\zeta = 0$, but still depend on $c$ (Eq. A4). Eq. P can be solved numerically for $c$ using Newton's method, the results of which are presented in Fig. 3 for a range of $\delta_1$.

When $\delta_1$ becomes large, the hypocellular interstitial gap between the tumor and host ($\xi_0$) becomes large as well. In such a case, wherever $\eta_1$ is nonzero, $\eta_2$ will be zero and *vice versa*. The dynamics of such a situation is described by Eq. G with $\eta_1 = 0$, *i.e.*, the well-studied Fisher equation (44) which has a propagation velocity $c = 2\sqrt{\rho_2\Delta_2}$. From Eq. A4, we find that as $\delta_1 \to \infty$, $\eta_1$ ($\zeta = 0$), and $\eta_1'$ ($\zeta = 0$) approach zero, Eq. P becomes $c = 2\sqrt{\rho_2\Delta_2}$ as expected. In Fig. 3 we show the value of the healthy tissue density at the tumor-host interface [$\eta_1$ ($\zeta = 0$)] *plotted versus* $\delta_1$, from which it can be seen that the healthy tissue has effectively decoupled from the tumor tissue by the point where $\delta_1 \approx 4$, after which tumor growth is determined using the Fisher equation.

In Table 3 we contrast values of the profile widths, interfacial propagation velocity, and tumor-host gap derived from the analytical results with those determined directly by the computer simulations. In each case the agreement is excellent.

## VI. Clinical Correlations with Model Predictions

The predictions of the mathematical and numerical solutions may be compared to experimental results and clinical observations. The prediction of the presence and approximate range of a pH gradient extending into peritumoral normal tissue is consistent with the data of Martin and colleague (29, 30). The predicted growth rates of benign and malignant tumors reasonably approximate clinical observation.

The mathematical solutions demonstrate the critical role of the biological parameters contributing to $\delta_1$ in the structure and dynamics

of the tumor-host interface. As discussed in "Section III," invasive (malignant) growth will occur only when $\delta_1 > 1$. However, the interfacial structure is not uniform in all malignant tumors. As shown in Fig. 3, the interface when $1 < \delta_1 < 3$ will generally consist of overlapping tumor and host tissue. This would result in an interface morphology in which the tumor is visibly penetrating into the normal tissue. This permeative pattern of tumor growth is commonly observed (37). The model also demonstrates that malignant tumors with a value of $\delta_1 \approx 4$ will have a well-defined, nonoverlapping interface. This also is frequently observed in pathological specimens (37). However, tumors in which $\delta_1 \gg 4$ are predicted to have an appreciable hypocellular interstitial gap between the advancing tumor and retreating normal tissue edges. The size of this gap will increase at a rate proportional to the logarithm of $\delta_1$ and therefore should be visible in at least some tumors. We could find no previous reports of the
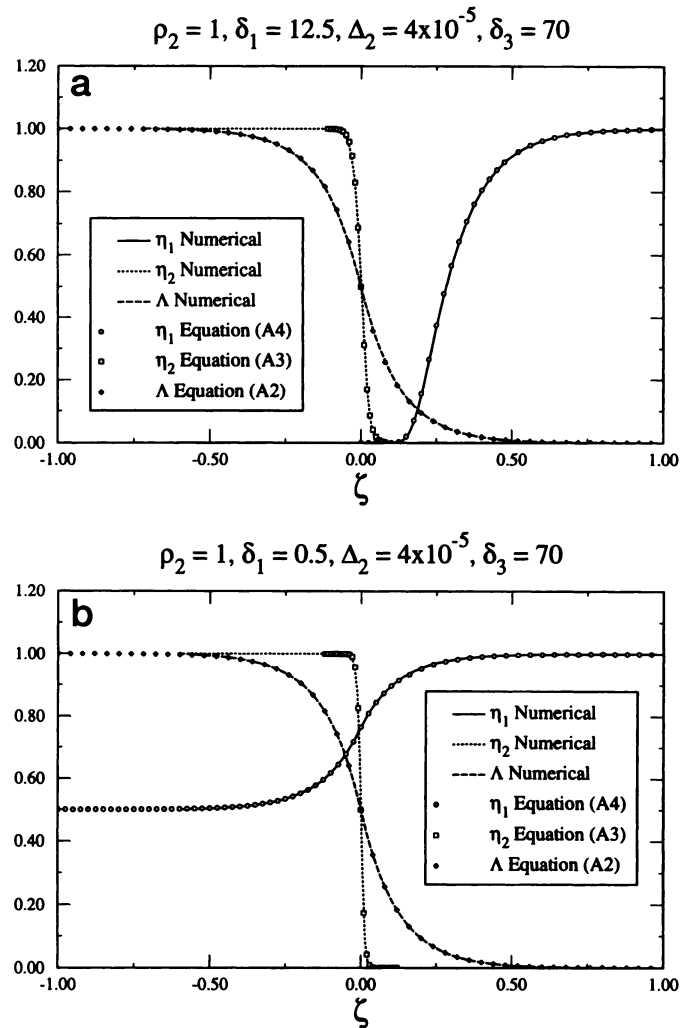


Fig. 2. Late-time ($\tau = 20$) wave front profiles for the $\delta_1 = 12.5$ case (*a*) and for the $\delta_1 = 0.5$ case (*b*). The curves are the results of the computer simulations, and the plotting symbols are the approximate analytical results given in the "Appendix." The wave fronts are propagating from *left to right* with speeds $c \approx 0.0128$ (0.03 mm/day) and $c \approx 0.0064$ (0.01 mm/day), respectively. Note the sharp tumor profile in both cases, the coexistence of tumor and healthy tissue behind the wave front for the $\delta_1 < 1$ case (*b*), and the formation of a tumor-host hypocellular interstitial gap for the $\delta_1 > 1$ case (*a*). At each time step, using Eqs. A5 and A6, we computed the position $E(\tau)$ of the wave front edge and its width $W(\tau)$ for each of the three fields. The wave front velocity was found using $c = dE(\tau)/d\tau$. For all three fields we found that, after sufficient time had elapsed to allow for the decay of transients ($\tau \approx 5$), the wave front velocity for each of the fields became constant and virtually identical to that of the remaining two. Detailed results for the wave front profile widths $W$, propagation velocity $c$, and tumor-host gap $\xi_0$ are summarized in Table 3.

5749

Table 3 *Comparison of computer simulations and analytical approximations for relevant biological quantities*

A summary of relevant biological quantities predicted by the model for two representative cases, $\delta_1 = 0.5$ (benign) and $\delta_1 = 12.5$ (malignant). The agreement between the computer simulations and the approximate analytical expressions is uniformly excellent. Convert lengths to mm by multiplication by 23.8; convert speeds to mm per day by multiplication by 2.03.

| | $\delta_1 = 0.5$ | | $\delta_1 = 12.5$ | |
| | Simulation | Approximation | Simulation | Approximation |
|---|---|---|---|---|
| $W_\Lambda$ | 0.169 | 0.168 Eq. M | 0.169 | 0.168 Eq. M |
| $W_{\eta 2}$ | 0.013 | 0.012 Eq. N | 0.024 | 0.023 Eq. N |
| $W_{\eta 1}$ | 0.168 | 0.171 Eq. A6$^a$ | 0.130 | 0.129 Eq. A6$^a$ |
| $c$ | 0.0064 | 0.0062 Eq. P | 0.0128 | 0.0126 Eq. P |
| $\xi_0$ | −0.008 | −0.008 Eq. A5$^a$ | 0.313 | 0.313 Eq. A5$^a$ |

$^a$ The analytical approximation results for $W_{\eta 1}$ and $\xi_0$ were determined by numerically integrating Eqs. A6 and A7 with $f(\xi)$ replaced by approximate solution for $\eta_1$ given in Eq. A4.
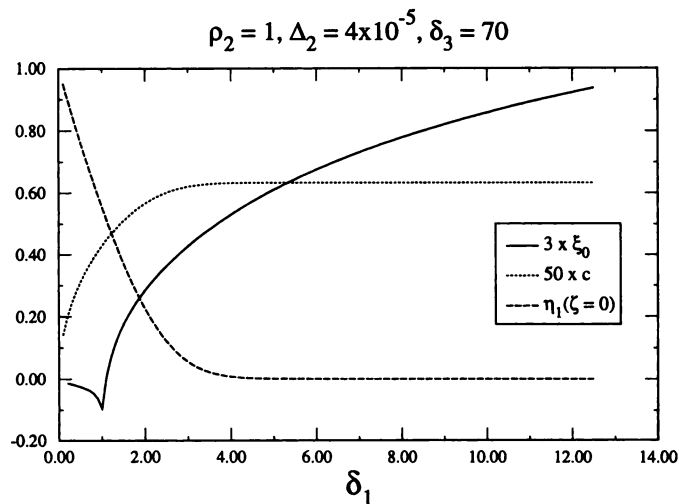


$$\rho_2 = 1, \Delta_2 = 4 \times 10^{-5}, \delta_3 = 70$$

Fig. 3. Tumor-host interstitial gap ($\xi_0$, ——), tumor-host interface propagation velocity ($c$ . . . . . ), and healthy tissue density at tumor-host interface [$\eta_1$ ($\zeta = 0$), – – –] as a function of $\delta_1$. For comparison, $\xi_0$ and $c$ have been scaled by multiplicative factors 3 and 50, respectively. Note that for $\delta_1$ less than approximately 1.1, the tumor edge leads the healthy tissue edge ($\xi_0 < 0$). At the benign-malignant crossover point, $\delta_1 = 1$, the healthy tissue density at the tumor-host interface is at 55% of its carrying capacity [$\eta_1$ ($\zeta = 0$) = 0.55], reflecting significant tissue overlap (see also Fig. 2b for the $\delta_1 = 0.5$ profiles). The tumor and host are decoupled for $\delta_1 > 4$, after which the interfacial velocity saturates at the Fisher equation limit of $c = 2\sqrt{\rho_2 \Delta_2}$.

predicted hypocellular interstitial gap at the tumor-host interface and therefore investigated this further.

To investigate this prediction, 21 pathological specimens from human squamous cell carcinoma of the head and neck were reviewed for evidence of a hypocellular interstitial gap as predicted by Fig. 3. Specimens were designated as positive if a hypocellular space of at least 10 $\mu$m was observed in at least 50% of the visualized tumor-host interfaces within that specimen. Using these criteria, 14 specimens were judged to show a hypocellular interstitial gap (67%). Three examples are shown in Fig. 4. The gaps ranged from approximately 10 $\mu$m to more than 150 $\mu$m; however, considerable variability in the size and appearance of the gap was observed both within different sections of the same tumor and in different tumors. Naked nuclei and poorly staining and morphologically disrupted normal cells were frequently observed scattered within the gap or at its edge (Fig. 4, *arrowhead*) as predicted by the mathematical model. The gap was found, although somewhat morphologically different, in tissue whether formalin fixed (Fig. 4a) or flash frozen (Fig. 4b).

Because of the possibility that the gap at the tumor-host interface represents an artifact of fixation, we examined the tumor-host interface *in vitro*. Briefly, the 4047 colon cancer was maintained *in vivo* by serially passing it in the subcutaneous tissues of the Fischer 344 rat (45). The tumor-host interface *in situ* was shown to be tumor cells and layers of fibroblasts with a moderate hypocellular interstitial gap. The tumor cells and the fibroblasts from the tumor edge were established
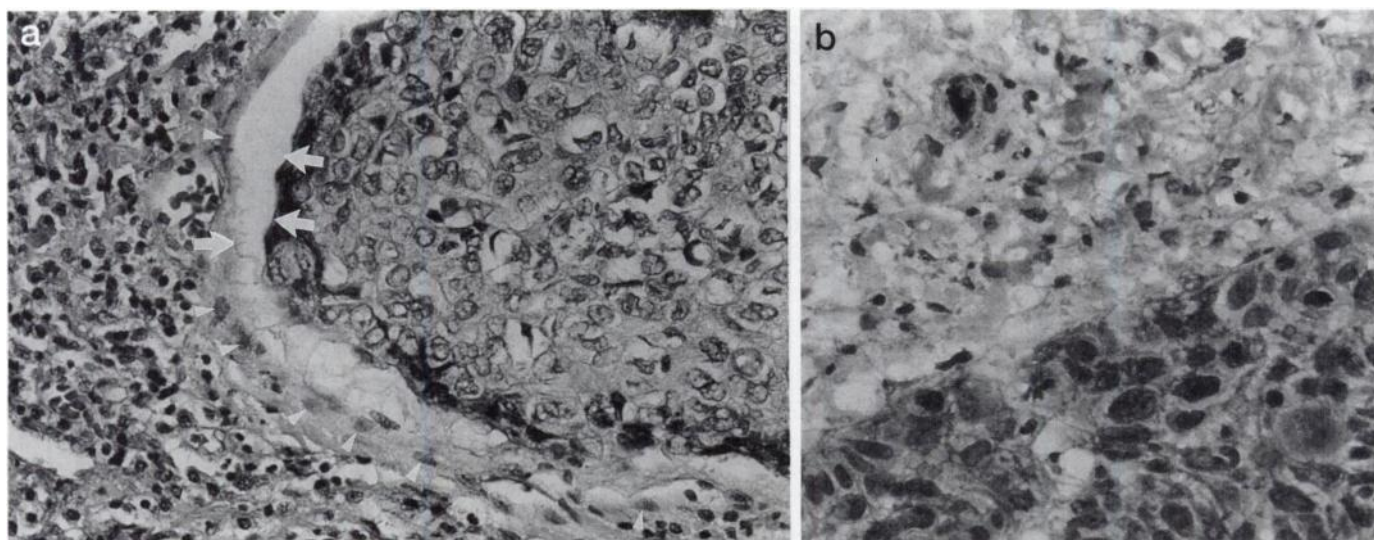


Fig. 4. H&E-stained micrographs of the tumor-host interface (*arrows*) in formalin-fixed (a) and flash-frozen specimens (b) from human squamous cell carcinomas of the head and neck. A hypocellular gap at the interface associated with disrupted normal cells (*arrowheads*) is identified (see "Section VI").
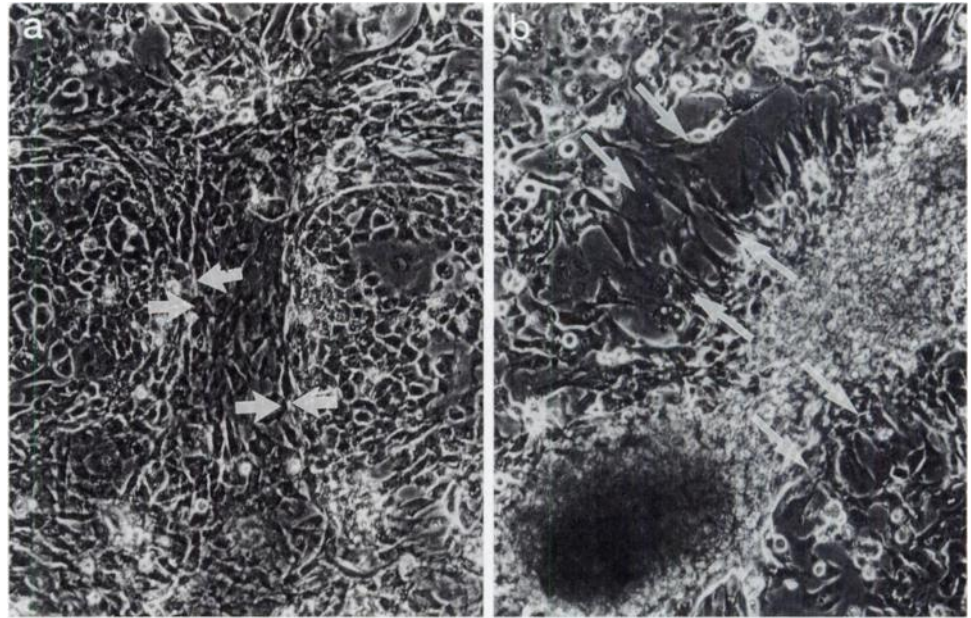
Fig. 5. Phase-contrast micrographs of an evolving *in vitro* tumor-host interface (*arrows*) at 113 h (*a*) and 136 h (*b*) after seeding. An acellular gap (*arrows, b*) develops coincident with tumor expansion.

in pure culture as described elsewhere (45). Equal numbers of the two populations were seeded in 35-mm plates and maintained in DMEM supplemented with 10% fetal bovine serum and antibiotics in an incubator at 37°C in 5% $CO_2$. The cocultures were observed daily with a phase-contrast microscope. Although the cultures were seeded as single-cell suspensions, they grew in a characteristic pattern with tumor cells gathering into nodules which were surrounded by the fibroblasts as shown in Fig. 5a. The populations coexisted, expanding steadily until the dish became confluent (Fig. 5a showing a coculture 113 h after seeding). Once the cells established a dense monolayer, the fibroblasts at the tumor margin were observed to fragment and lift off of the surface of the dish as shown in Fig. 5b, which is the same coculture as in Fig. 5a but at 136 h after seeding. This resulted in the formation of a hypocellular interstitial gap similar to that found *in vivo* (Fig. 4b, *arrowheads*).

The presence of the gap in unfixed *in vitro* experiments and in flash-frozen tissue suggests this phenomenon is not an artifact (of, *e.g.*, fixation), although we cannot exclude that possibility entirely.

Because $\delta_1$ controls the interfacial structure and the speed of tumor growth (Fig. 3), the mathematical model explicitly predicts that the characteristics of the tumor-host interface will have prognostic significance. The specific predictions are somewhat counterintuitive: a tumor-host interface which is infiltrative (*i.e.*, having a small region of overlap between neoplastic and normal tissue) indicates a better prognosis than one having a well-defined, sharp interface. Finally, the formation of a hypocellular interstitial gap indicates a poorer prognosis than the sharp interface, and the prognosis worsens as the size of the gap increases. This prediction should be readily testable in prospective or retrospective clinical studies.

## VII. Conclusions

We demonstrate that transformation-induced reversion to glycolytic metabolism provides a mechanism for invasive tumor growth which, although conceptually simple, yields complex interactions consistent with many aspects of cancer biology.

A mathematical model encompassing the key components of the hypothesis predicts an acidic pH gradient extending into the peritumoral normal tissue, which we have confirmed by reanalysis of extant experimental data. We demonstrate that the normal mammalian cells,

but not tumor cells, are intolerant of acidic interstitial pH in the range typically found within this gradient.

The model predicts crossover behavior consistent with clinical observation of noninvasive tumor growth (such as adenoma and carcinoma *in situ*) preceding the development of an invasive phenotype. Furthermore, critical parameters controlling this transition, such as the acquisition of angiogenesis, are consistent with experimental and clinical observations.

Finally, the mathematical model predicts a variable interfacial structure, including a previously unrecognized hypocellular interstitial gap in some malignancies. We show evidence in support of this prediction in both clinical observations and *in vitro* experiments. The model predicts a strong correlation between the interfacial structure and the tumor growth velocity (and thus patient prognosis) which can be readily tested.

We believe that this approach may provide a simple but complete framework for understanding invasive cancer within the context of cellular properties induced by transformation. New approaches to tumor evaluation and therapy based on this model should be possible. Therefore, we believe that further clinical and experimental work to confirm or refute its predictions is warranted.

## VIII. Appendix: Approximate Analytical Solutions of the Model Equations

We seek analytical approximations for the interfacial profile structures and their dependence on the wave front propagation velocity. The approximations we make result from two reasonable assumptions: that the tumor edge is sharp and that the wave front propagation velocity is small. It is natural to expect the tumor edge to be sharp since the logistic growth of the neoplastic population within a spatial domain far outstrips its diffusive flux out of that domain ($\rho_2 \gg \Delta_2$). That it should also be sharp on the length scale of the widths of $\eta_1$ and $\Lambda$

5751

is also reasonable; the large chemical diffusion of $\Lambda$ affords its deep penetration into the surrounding healthy tissue, causing a decrease in $\eta_1$ on the same length scale as the penetration depth of $\Lambda$ into $\eta_1$. The latter occurs on a time scale much shorter than that of diffusion of neoplastic tissue into the resulting interstitial space. That the wave front propagation velocity $c$ is small follows from the fact that, for biological systems, the time scale associated with the cellular diffusion constant is much longer than that associated with any cellular growth rates or chemical diffusion.

We now look for traveling wave solutions to Eqs. F–H. We begin by assuming the existence of solutions having the form $f(\xi, \tau) = f(\xi - c\tau)$, where $f$ is either $\eta_1$, $\eta_2$, or $\Lambda$, *i.e.*, each field has some wave front profile, $f$, propagating in the $+\xi$ direction at velocity $c$. Substituting these forms into Eqs. F–H gives a new system of ordinary differential equations:

$$-c\eta_1' = \eta_1(1 - \eta_1) - \delta_1 \Lambda \eta_1$$

$$-c\eta_2' = \rho_2 \eta_2(1 - \eta_2) + \Delta_2[(1 - \eta_1)\eta_2'' - \eta_1'\eta_2']$$

$$-c\Lambda' = \delta_3(\eta_2 - \Lambda) + \Lambda'' \qquad (A1)$$

where the primes denote differentiation with respect to the co-moving coordinate $\zeta = \xi - c\tau$.

Using only the assumption that $\Delta_2 \ll \rho_2$,[7] and therefore a sharp tumor profile edge and small propagation velocity, we were able to solve[6] Eq. A1 for the $\Lambda$ ($\zeta$), $\eta_2$ ($\zeta$), and $\eta_1$ ($\zeta$) profiles:

$$\Lambda(\zeta) = \begin{cases} 1 - \dfrac{1}{2}\exp(\sqrt{\delta_3}\zeta) & \zeta < 0 \\[2mm] \dfrac{1}{2}\exp(-\sqrt{\delta_3}\zeta) & \zeta \geq 0 \end{cases} \qquad (A2)$$

$$\eta_2(\zeta) = \frac{1}{1 + \exp(\rho_2\zeta/c)} \qquad (A3)$$

and

$$\eta_1(\zeta) = \begin{cases} \dfrac{c\exp[-pe^{q\zeta} + s\zeta]p^{s/q}q}{\gamma(r/q,\, pe^{-q\zeta})} & \zeta < 0 \\[4mm] \dfrac{c\exp[-pe^{-q\zeta} - r\zeta]p^{r/q}q}{\gamma(r/q,\, p)p^{(s-r)/q} + \gamma(s/q,\, p) - \gamma(s/q,\, pe^{q\zeta})} & \zeta \geq 0 \end{cases} \qquad (A4)$$

where $p = \delta_1/(2c\sqrt{\delta_3})$, $q = \sqrt{\delta_3}$, $r = 1/c$, and $s = (\delta_1 - 1)/c$. $\gamma(a, x) = \int_0^x e^{-t}t^{a-1}dt$ is an incomplete $\gamma$ function.

In Fig. 2 these approximate analytical solutions are plotted at a number of select values of $\zeta$ ($\square$, Eq. A2 for $\Lambda$; $\bigcirc$, Eq. A4 for $\eta_1$; and $\Diamond$, Eq. A3 for $\eta_2$). Plotting Eqs. A3 and A4 in Fig. 2 required values of $c$. These were taken to be the values found in the simulations themselves which, in turn, agree very well with the analytical determination for $c$ in terms of the basic system parameters (Eq. P) presented in "Section V." The error between these approximate solutions and the numerical results is everywhere $<0.1\%$.

There are a variety of ways one could define the position and width of the wave front profiles. Noting that the spatial gradients of the wave front profiles are sharply peaked functions, we define the edge position $E(\tau)$ and width $W(\tau)$ of a profile by:

$$E_f(\tau) = \frac{\displaystyle\int_{-\Xi}^{\Xi} \xi \frac{\partial}{\partial\xi} f(\xi, \tau)\, d\xi}{\displaystyle\int_{-\Xi}^{\Xi} \frac{\partial}{\partial\xi} f(\xi, \tau)\, d\xi} \qquad (A5)$$

and

$$W_f^2(\tau) = \frac{\displaystyle\int_{-\Xi}^{\Xi} [\xi - E_f(\tau)]^2 \frac{\partial}{\partial\xi} f(\xi, \tau)\, d\xi}{\displaystyle\int_{-\Xi}^{\Xi} \frac{\partial}{\partial\xi} f(\xi, \tau)\, d\xi} \qquad (A6)$$

where $f$ is either the $\eta_1$, $\eta_2$, or $\Lambda$ profile. Eqs. A5 and A6 were used for defining the position and width of the profiles in both the computer simulations and, when the integrals could be obtained in closed form, in the approximate analytical results.

## References

1. Fidler, I. J., and Hart, I. R. Biological diversity in metastatic neoplasm: origins and implications. Science (Washington DC), *21:* 998–1003, 1982.
2. Fearson, E. R., Hamilton, S. R., and Vogelstein, B. Clonal analysis of human colorectal rumors. Science (Washington DC), *238:* 193–197, 1987.
3. Bishop, J. M. The molecular genetics of cancer. Leukemia (Baltimore), *2:* 199–208, 1988.
4. Korczak, B., Robson, I. B., Lamarche, C., Bernstein, A., and Karbel, R. S. Genetic tagging of tumor cells with retrovirus vectors: clonal analysis of tumor growth and metastasis *in vivo.* Mol. Cell. Biol., *8:* 3143–3149, 1988.
5. Elder, D. E., Rodek, U., Thurin, J., Cardillo, F., Clark, W. H., Stewart, R., and Herlyn, M. Antigenic profile of tumour progression stages in human melanocytic nevi and melanomas. Cancer Res., *49:* 5091–5096, 1989.
6. Volpe, J. G. P. Genetic instability of cancer: why a metastacic tumor is unstable and a benign tumor is stable. Cancer Genet. Cytogenet., *14:* 125–134, 1988.
7. Clarke, R., Dickson, R. G., and Brunner, N. The process of malignant progression in human breast cancer. Ann. Oncol., *1:* 401–407, 1990.
8. Chang, K. W., Laconi, S., Mangold, K. A., Hubchak, S., and Scarpelli, D. G. Multiple genetic alterations in hamster pancreatic ductal adenocarcinomas. Cancer Res., *55:* 2560–2568, 1995.
9. Sutherland, R. M., Rasey, J. S., and Hill, R. P. Tumor biology. Am. J. Clin. Oncol., *11:* 253–274, 1988.
10. Warburg, O. The Metabolism of Tumors (English translation by F. Dickens). London: Constable Press, 1930.
11. Gatenby, R. A. Population ecology issues in tumor growth. Cancer Res., *51:* 2542–2547, 1991.
12. Gatenby, R. A. The potential role of transformation-induced metabolic changes in tumor-host interaction. Cancer Res., *55:* 4151–4155, 1995.
13. Gatenby, R. A. The potential role of FDG-PET imaging in understanding tumor-host interaction. J. Nucl. Med., *6:* 893–899, 1995.
14. Yonekura, Y., Benua, R. S., and Brill, A. B. Increased accumulation of 2-deoxy-2[18F]fluoro-D-glucose in liver metastasis from colon cancer. J. Nucl. Med., *23:* 1133–1137, 1982.
15. Hawkins, R. A., Hoh, C., Glaspy, J., Cho, Y., Dahlbom, M., Rege, S., and Messa, C. The role of positron emission tomography in oncology and other whole-body applications. Semin. Nucl. Med., *22:* 268–284, 1992.
16. Jabour, B. A., Choi, Y., Ooh, C. K., Rege, S. D., Soong, J. L., Lufkin, R. B., Hanafee, W. M., Maddhi, J., and Chaiken, L. Extracranial head and neck tumors: PET imaging with 2-[F-18]fluoro-2-deoxy-D-glucose. Radiology, *186:* 27–35, 1993.
17. Heinz, A., Sachs, G., and Schafe, J. A. Evidence for activation of an active electrogenic pump in Ehrlich ascites tumor cells during glycolysis. J. Membr. Biol., *61:* 143–153, 1981.
18. Kallinowski, F., Vaupel, P., Runkel, S., Berg, G., Fortmeyor, S., Baessler, K. H., Wagner, K., Mueller, W., and Walenta, S. Glucose uptake, lactate release, ketone body turnover, metabolic micromilieu and pH distribution in human breast cancer xenografts in nude mice. Cancer Res., *48:* 7264–7272, 1988.
19. Ashby, B. S. pH studies in human malignant tumours. Lancet, *2:* 312–315, 1966.
20. Griffiths, J. R. Are cancer cells acidic? Br. J. Cancer, *64:* 425–427, 1991.
21. Gillies, R. J., Liu, A., and Bhujwalla, A. 31P-MRS measurements of extracellular pH of tumors using 3-aminopropyl phosphate. Am. J. Physiol., *36:* C195–C203, 1994.
22. Stubbs, M., Rodrigues, L., Howe, F. A., Wang, J., Joong, K. S., Veech, R., and Griffin, J. R. Metabolic consequences of a reversed pH gradient in rat tumors. Cancer Res., *54:* 4011–4016, 1994.
23. Rubin, H. J. pH and population density in the regulation of animal cell multiplication. J. Cell Biol., *51:* 686–702, 1971.
24. DeHemptinne, A., Marrannes, R., and Vanheel, V. Surface pH and the control of intracellular pH in cardiac and skeletal muscle. Can. J. Physiol. Pharmacol., *65:* 970–977, 1986.
25. Gerweck, L. E., and Fellenz, M. P. The simultaneous determination of intracellular pH and cell energy status. Radiat. Res., *125:* 257–261, 1991.
26. Spriet, L. L. Phosphofructokinase activity and acidosis during short term tetanic contractions. Can. J. Physiol. Pharmacol., *69:* 298–304, 1991.
27. Casciari, J. J., Otirchos, S. V., and Sutherland, R. M. Variations in tumor growth rates and metabolism with oxygen concentration, glucose concentration, and extracellular pH. J. Cell Physiol., *151:* 386–394, 1992.
28. Dairkee, S. H., Deng, G., Stampfer, M. R., Waldman, R. M., and Smith, H. S. Selective cell culture of primary breast cancer. Cancer Res., *35:* 2516–2519, 1995.
29. Martin, G. R., and Jain, R. K. Noninvasive measurement of interstitial pH profiles in

[7] This is always the case as $\rho_2 = r_2/r_1 \sim O(1)$ and $\Delta_2 = D_2/D_3 \sim O(10^{-5})$.

normal and neoplastic tissue using fluorescent ration imaging microscopy. Cancer Res., *54:* 5670–5674, 1994.

30. Martin, G. R. Ph.D. Thesis. Pittsburgh, PA: Carnegie Mellon University, Pittsburgh, 1995.
31. Rozhin, J., Saeni, M., Ziegler, G., and Sloane, B. F. Pericellular pH affects distribution and secretion of cathepsin B in malignant cells. Cancer Res., *54:* 6517–6525, 1994.
32. Benner, M., Versellis, V., White, R., and Spray, D. Gap junctional conductance. *In:* E. L. Hertzberg and R. G. Johnson (eds.), Gap Junctions, pp. 287–304. Alan R. Liss, Inc., 1988.
33. Yamaski, H. Gap junctional intercellular communication and carcinogenesis. Carcinogenesis (Lond.), *11:* 1051–1058, 1990.
34. Murray, J. D. Mathematical Biology, Chap. 11. Berlin: Springer-Verlag, 1993.
35. Farber, E., and Cameron, C. The sequential analysis of cancer development. Adv. Cancer Res., *31:* 125–226, 1980.
36. Campion, M. J., McCance, D. J., Cuzik, J., and Singer, A. Progressive potential of mild cervical atypia: a prospective cytological, colposcopic, and virological study. Lancet, *2:* 237–240, 1986.
37. Cotran, R. S., Kumar, V., and Robbins, S. L. Robbins Pathologic Basis of Disease, 4th ed., pp. 243–248. Philadelphia: W. B. Saunders, 1989.
38. Folkman, J., Watson, K., Ingber, D., and Hanahan, D. Induction of angiogenesis during the transition from hyperplasia to neoplasia. Nature (Lond.), *339:* 58–61, 1989.
39. Folkman, J. The role of angiogenesis in tumor growth. Cancer Biol., *3:* 65–71, 1992.
40. Dee, G., and Langer, J. S. Propagating pattern selection. Phys. Rev. Lett., *50:* 383–386, 1983.
41. Ben-Jacob, E., Brand, H., Dee, G., Kramer, L., and Langer, J. S. Pattern propagation in non-linear dissipative systems. Physica, *14D:* 348–364, 1985.
42. Van Saarloos, W. Dynamical velocity selection: marginal stability. Phys. Rev. Lett., *58:* 2571–2574, 1987.
43. Van Saarloos, W. Propagation into unstable states: marginal stability as a dynamical mechanism for velocity selection. Phys. Rev., *37A:* 211–229, 1988.
44. Aronson, D. G., and Weinberger, H. F. Multidimensional nonlinear diffusion arising in population genetics. Adv. Math., *30:* 33–76, 1978.
45. Gatenby, R. A., and Taylor, D. D. Suppression of wound healing in tumor bearing animals as a model for tumor-host interaction: mechanism of suppression. Cancer Res., *50:* 7997–8001, 1990.
46. Tracqui, P., Cruywagen, G. C., Woodward, D. E., Bartor, G. T., Murray, J. D., and Alvord, E. C. A Mathematical model of glioma growth: the effect of chemotherapy on spatio-temporal growth. Cell Proliferation, *28:* 17–31, 1995.
47. Dale, P. D., Sherratt, J. A., and Maini, P. K. The speed of corneal epithelial wound healing. Appl. Math. Lett., *7:* 11–14, 1994.
48. Lide, D. R., (ed.) CRC Handbook of Chemistry and Physics. Boca Raton, FL: CRC Press, 1994.

**American Association
for Cancer Research**

# A Reaction-Diffusion Model of Cancer Invasion

Robert A. Gatenby and Edward T. Gawlinski

| | |
|---|---|
| **Updated version** | Access the most recent version of this article at: <br> http://cancerres.aacrjournals.org/content/56/24/5745 |

| | |
|---|---|
| **E-mail alerts** | Sign up to receive free email-alerts related to this article or journal. |
| **Reprints and Subscriptions** | To order reprints of this article or to subscribe to the journal, contact the AACR Publications Department at pubs@aacr.org. |
| **Permissions** | To request permission to re-use all or part of this article, contact the AACR Publications Department at permissions@aacr.org. |